Gravitational self-lensing in populations of massive black hole binaries

Luke Zoltan Kelley [1,2]★ Daniel J. D'Orazio [3] and Rosanne Di Stefano [4,5]

[1]*CIERA (Center For Interdisciplinary Exploration And Research In Astrophysics), 1800 Sherman Ave, Evanston, IL 60201, USA*
[2]*Department of Physics and Astronomy, Northwestern University, 2145 Sheridan Road, Evanston, IL 60208, USA*
[3]*Niels Bohr International Academy, Niels Bohr Institute, Blegdamsvej 17, DK-2100 Copenhagen, Denmark*
[4]*Smithsonian Astrophysical Observatory, 60 Garden Street, Cambridge, MA 02138, USA*
[5]*Astronomy Department, Harvard University, 60 Garden Street, Cambridge, MA 02138, USA*

ABSTRACT
The community may be on the verge of detecting low-frequency gravitational waves from massive black hole binaries (MBHBs), but no examples of binary active galactic nuclei (AGN) have been confirmed. Because MBHBs are intrinsically rare, the most promising detection methods utilize photometric data from all-sky surveys. Gravitational self-lensing has recently been proposed as a method of detecting AGN in close separation binaries. In this study, we calculate the detectability of lensing signatures in realistic populations of simulated MBHBs. Within our model assumptions, we find that VRO's LSST should be able to detect tens to hundreds of self-lensing binaries, with the rate uncertainty depending primarily on the orientation of AGN discs relative to their binary orbits. Roughly a quarter of lensing detectable systems should also show detectable Doppler boosting signatures. If AGN discs tend to be aligned with the orbit, lensing signatures are very nearly achromatic, while in misaligned configurations, the bluer optical bands are lensed more than redder ones. Whether substantial obscuring material (e.g. a dusty torus) will be present in close binaries remains uncertain, but our estimates suggest that a substantial fraction of systems would still be observable in this case.

Key words: accretion, accretion discs – gravitational lensing: micro – gravitational waves – quasars: general – X-rays: binaries.

1 INTRODUCTION

Binaries of massive black holes (MBHs) are expected to be formed following the merger of their host galaxies (Begelman, Blandford & Rees 1980). These binaries are promising sources of low-frequency gravitational waves (GWs) that will be detectable by pulsar timing arrays (Detweiler 1979; Hellings & Downs 1983; Foster & Backer 1990). In particular, the GW signal from the ensemble of MBH binaries (MBHBs) across the universe – the stochastic GW background (Rajagopal & Romani 1995; Jaffe & Backer 2003; Wyithe & Loeb 2003; Sesana et al. 2004) – may be starting to emerge in recent pulsar timing array data (Arzoumanian et al. 2020b).

A wide array of possible electromagnetic signatures of accreting, sub-pc MBHBs have been proposed (see Burke-Spolaor 2013; Bogdanović 2015; De Rosa et al. 2019, for reviews), but no observational examples of MBHBs in active galactic nuclei (AGNs) have been confirmed. Because MBHBs are intrinsically rare ($\sim 10^{-3}$ AGN^{-1}; Kelley et al. 2019b), signatures that can be detected in large surveys, particularly with photometric data alone, are especially promising. For example, a growing number of candidate MBHBs have been identified based on apparent periodicity in AGN light curves (Graham et al. 2015; Charisi et al. 2016; Liu et al. 2019; Chen et al. 2020).[1] The Vera Rubin Observatory (VRO) Legacy Survey of Space and Time (LSST; Ivezić et al. 2019), which is expected to begin in

roughly 2024, will vastly increase the sample size of time-domain AGN observations and revolutionize both AGN and binary-AGN astrophysics.

D'Orazio & Di Stefano (2018) consider the photometric signatures of one MBH in a binary gravitationally (micro-)lensing a companion[2] AGN. More recently, Ingram et al. (2021) explore a possible connection between self-lensing and quasi-periodic eruptions (QPEs) in AGN, and perform careful modelling of X-ray self-lensing flares. In addition to the rarity of binary AGN, detectable 'self-lensing' systems are made even more infrequent by necessitating nearly edge-on binary orientations to produce sufficiently close angular separations. In this paper, we explore the properties and detectability of optical lensing signatures in simulated populations of MBHBs (Kelley, Blecha & Hernquist 2017a; Kelley et al. 2019b), where we consider full distributions of binary parameters.

Our models are based on the Illustris cosmological hydrodynamic simulations (Vogelsberger et al. 2014b) that provide self-consistently derived populations of MBHs (Sijacki et al. 2015) in merging galaxies along with their fully co-evolved stellar, gaseous, and dark matter content. The MBH from merging galaxies are evolving in post-processing using sophisticated models of binary evolution based on the radial phase-space distributions of material in post-merger galaxies. Our binary models include dynamical friction, loss-cone

---

★ E-mail: lzkelley@northwestern.edu
[1]cf. Sesana et al. (2018) and Kelley et al. (2019b).

[2]An approach also suggested for identifying compact remnants and planets in stellar systems (e.g. Maeder 1973; Mao & Paczynski 1991; Gould & Loeb 1992; Beskin & Tuntsov 2002; Rahvar, Mehrabi & Dominik 2011).

stellar scattering (with parametrized refilling), circumbinary disc torques based on evolving MBH accretion rates, and GW emission.

A large number of uncertainties remain, particularly governing the dynamics of the accretion discs surrounding MBH binaries once they reach sub-pc scales. A general consensus model is beginning to take shape (Paczynski 1977; Artymowicz & Lubow 1994, 1996; Gould & Rix 2000; Armitage & Natarajan 2002; Hayasaki, Mineshige & Sudou 2007; Roedig et al. 2011; Duffell et al. 2014; Farris et al. 2014; D'Orazio et al. 2016; Muñoz, Miranda & Lai 2019), though the results of modern, high-resolution, and long-duration simulations are finding results significantly different from those of earlier studies. The emerging picture, based largely on the results of 2D idealized hydrodynamic simulations, is that of a circumbinary accretion disc in which a central low-density cavity ('gap') is cleared by the presence of the orbiting binary. Around each MBH component, a circumsingle disc forms, fed by accretion streams entering the cavity from the circumbinary disc. In close binaries, once the dynamical time and even binary evolution time-scale are shorter than the viscous time, the accretion is dynamically driven and can continue throughout inspiral (Farris et al. 2015). Hydrodynamic simulations show that accretion tends to favour the lower mass component, and vary periodically near a few times the orbital period. The effects of varying eccentricity (e.g. Muñoz et al. 2019; D'Orazio & Duffell 2021; Zrake et al. 2021) and more complex geometries (e.g. Moody, Shi & Stone 2019) are beginning to be explored in simulations, but detailed thermal structures, realistic cooling and feedback effects, magnetic fields and self-consistently derived viscosity (cf. Shi & Krolik 2015; Noble et al. 2021), and other factors have yet to be explored on time-scales that probe important secular processes.

Even individual AGN are complex and characterized by large intrinsic time-variability (Barr & Mushotzky 1986; Hook et al. 1994; Ulrich, Maraschi & Urry 1997; Kelly, Bechtold & Siemiginowska 2009; MacLeod et al. 2010), and particularly by substantial variance across populations (e.g. historically, Seyfert 1943; Fanaroff & Riley 1974). In the 'unified AGN' paradigm (Antonucci 1993; Urry & Padovani 1995; Fossati et al. 1998), accretion rate and especially viewing angle are believed to be the primary drivers of phenomenological differences. It is generally believed that accretion flows are only able to effectively cool, become geometrically thin, optically thick, and radiatively efficient for $10^{-2} \lesssim f_{Edd} \equiv \dot{M}/\dot{M}_{Edd} \lesssim 1$. These systems thus dominate most observational (particularly near-optical) populations. Within the thin disc, Shakura & Sunyaev (1973) (and similar) models, the temperature of radiating gas decreases farther away from the MBH, leading to stratified emission with bluer bands emitted closer in. The optical emission from AGN is observed to vary significantly in brightness, over time-scales as short as the light-crossing time of the disc at small radii. At large radii, outside of a characteristic sublimation radius (typically $10^{-2} \lesssim r/pc \lesssim 10$), dust forms and the accretion flow becomes geometrically thick (Barvainis 1987; Suganuma et al. 2006; Netzer 2015). This 'dusty torus' obscures the bright inner disc for viewing angles near the disc plane.

Much of the detailed structure and dynamics of AGN accretion flows and emission are only broadly agreed upon qualitatively, with substantial variations existing between different models. In this analysis, we combine detailed models of MBH binary populations (Section 2.1) with analytic Shakura–Sunyaev discs (Section 2.2), and models for lensing (Section 2.3) and Doppler variability (Section 2.4). To assess detectability, we adopt a largely phenomenological approach based on observed AGN variability (Section 2.5) and typical survey parameters (Section 2.6). In our results, we highlight expected detection rates, observable population properties, and the

plausible characteristics of lensing signatures. In our discussion, we focus on the key assumptions and uncertainties included in our models, some of the important systematics external to our analysis, and speculate on some possible use cases of eventual self-lensing detections.

2 METHODS

2.1 MBH binary populations

We use populations of MBHBs derived from the Illustris cosmological hydrodynamical simulations that self-consistently co-evolve thousands of galaxies and their central black holes in a fixed comoving volume of $[106.5\,Mpc]^3$ (Genel et al. 2014; Torrey et al. 2014; Vogelsberger et al. 2014a)[3] MBH 'seeds' of mass 1.4×10^5 M$_\odot$ are placed in the centre of dark-matter haloes once their mass exceeds 7×10^{10} M$_\odot$. The black holes then grow through accretion, calculated using a local Bondi-rate estimator, and through mergers with other MBHs. Black hole particles are artificially fixed to the centres of their host galaxies to avoid spurious scattering from star and dark-matter particles. The resulting MBH population, described in detail in Sijacki et al. (2015), has properties matching local MBH–galaxy scaling relations (such as M–M_{bulge}), the inferred local mass-density of MBHs, and produce accretion luminosities consistent with the observed quasar luminosity function.

In the Illustris simulations, once two MBH particles come within a gravitational softening length[4] of one another (typically ~0.1–10 kpc), they are combined into a single MBH remnant. Physically, the binary merger process from ~10^3 pc down to actual coalescence at $\lesssim 10^{-3}$ pc involves complex dynamical interactions with the nuclear environments of the post-merger host galaxy (Begelman et al. 1980). We incorporate these dynamics using semi-analytic binary evolution models developed in Kelley et al. (2017a,b, 2019b). Each MBH 'merger' is identified in the output of the Illustris simulations, and its binary evolution is modelled in post-processing. In addition to the basic MBH parameters (the masses, redshift, and separation at the time of numerical-merger), the radial density and velocity profiles are calculated for the gas, stars, and dark matter in the post-merger host galaxy. These profiles are then used to calculate binary 'hardening' rates (da/dt) due to dynamical friction (Chandrasekhar 1943; Binney & Tremaine 1987), 'loss-cone' stellar scattering (Magorrian & Tremaine 1999; Merritt 2013), circumbinary disc torques (Gould & Rix 2000; Haiman, Kocsis & Menou 2009), and GW emission (Peters 1964). Note that throughout this analysis we restrict ourselves to circular orbits.

The results of this modelling are binary evolution histories for ~10^4 binaries with total masses between $\approx 10^6$ and 10^{10} M$_\odot$. These binaries represent those in a finite volume, evolving over all redshifts. From this sample, the total number of binaries in the observer's light-cone can be calculated (see section 2.3 of Kelley et al. 2019b). To construct a full population, we use kernel density estimation to 'resample with variation' for an arbitrary number of stochastic realizations of the universe (Kelley 2021b). The parameters of the full population[5] are shown in Fig. A2.

---

[3] The Illustris data, including MBH populations, are publicly available online: www.illustris-project.org (Nelson et al. 2015).

[4] An effective minimum size-scale for gravitational interactions, used to avoid spurious strong-scattering events.

[5] One realization of which is available online, zenodo.4068485 (Kelley 2020)

We review some of the key features of the binary population here, but see Kelley et al. (2017a) for a detailed description. The total mass and mass-ratio of binary systems are strongly anticorrelated. This is partially due to selection effects – because we only consider MBH components with $m_i > 10^6$ M$_\odot$, extreme mass ratios can only occur in the most massive systems – and partially cosmological as very massive elliptical galaxies tend to experience a large number of minor/extreme mergers with satellites (Rodriguez-Gomez et al. 2015). To a degree, this is counter balanced by the tendency of extreme mass-ratio mergers to *stall*, largely in the ∼kpc regime where dynamical friction can become ineffective, especially due to tidal-stripping of the secondary galaxy (see also Tremmel et al. 2018). Overall, binaries that are both more massive and nearer equal mass are more effective at reaching the bound binary stage ($\lesssim 10$ pc), and eventually coalescing. As binaries harden from pc-scales to Mpc (orbital periods of ∼yr), the 'residence time' ($\tau = a/(\mathrm{d}a/\mathrm{d}t)$) rapidly decreases, meaning that the expected number of systems rapidly declines at smaller separations.[6] Thus, the vast majority of binary systems will always tend to be at the largest orbital periods being considered.

It is important to note that most of our understanding of MBH binary evolution remains highly uncertain. The populations used here are part of an emerging concordance model that, however, remains untested. Ultimately, the EM signatures of binarity (such as self-lensing), are crucial for challenging the results of these models and thereby validating or constraining the underlying physical processes. In the last decade, for example, the general consensus has become that asymmetries in galactic potentials can sufficiently refill the stellar loss-cone and thereby solve the 'final parsec problem' (e.g. Khan, Just & Merritt 2011; Vasiliev, Antonini & Merritt 2015). Currently, one of the largest uncertainties in binary evolution is the torques from circumbinary accretion discs. While previously invoked as a final-pc solution, numerous recent studies have found that torques can *add* instead of *subtract* angular momentum (Miranda, Muñoz & Lai 2017; Moody et al. 2019; Muñoz et al. 2019; Duffell et al. 2020), possibly slowing or even hindering inspiral under certain conditions.

2.2 Accretion disc model

As in D'Orazio & Di Stefano (2018) and Kelley et al. (2019b), we use the standard Shakura & Sunyaev (1973) thin-disc emission model, where the temperature of the disc as of function of radius r is calculated as

$$\sigma T^4 = \frac{3Gm_i\dot{m}_i}{8\pi r^3}\left[1 - \left(\frac{r_{\mathrm{ISCO},i}}{r}\right)^{1/2}\right]. \qquad (1)$$

Here σ is the Stefan–Boltzmann constant, $\dot{m}_i$ is the accretion rate in the disc around an MBH with mass m_i, $r_{\mathrm{ISCO},\,i} \equiv 3r_{s,\,i} = 6Gm_i/c^2$ is the inner-most stable circular orbit (ISCO; assuming the spin of the MBH is zero). The rest-frame spectral luminosity, in the presence of a magnification field $\mathcal{M}$, is then found by integrating the Planck function $B_\nu(T)$,

$$L_\nu = \pi \sin(I_{\mathrm{disc}}) \int_0^{2\pi}\int_0^\infty B_\nu(T)\,\mathcal{M}(r,\phi)\,r\,\mathrm{d}r\,\mathrm{d}\phi. \qquad (2)$$

In the absence of lensing, $\mathcal{M} = 1$.

Here the inclination of the disc relative to the observer is I_{disc}, with $I_{\mathrm{disc}} = \pi/2$ corresponding to a face-on disc. Basic angular momentum arguments suggest that the inclination of the secondary

AGN disc should be aligned with that of the binary orbit, i.e. $I_{\mathrm{disc}} \approx I_{\mathrm{orb}}$. In dedicated circumbinary disc simulations, this is more often an assumption than a result, and indeed models that consider misaligned feeding of the circumbinary disc from large scales, and higher order precession and non-coplanar torques (e.g. Lense–Thirring precession; Bardeen & Petterson 1975) suggest that misaligned inclinations (i.e. $I_{\mathrm{disc}} \neq I_{\mathrm{orb}}$) are possible in single (e.g. Nixon et al. 2012; Liska et al. 2019) and binary (e.g. Nixon, King & Price 2013) systems. In our analysis, we explore the implications of both aligned and misaligned geometries.

We assume there is no disc within the ISCO, and the outer edge of the disc is set by the Hill radius (Eggleton 1983),

$$R_{\mathrm{Hill},i} = a\,\frac{0.49\,q_i^{2/3}}{0.6\,q_i^{2/3} + \ln\left(1 + q_i^{1/3}\right)}. \qquad (3)$$

Here a is the semi-major axis, and q_i is the ratio of object i's mass to that of the other (e.g. $q = q_2 = m_2/m_1$).

Our MBH population from Illustris includes accretion rates derived from the local galaxy gas properties at the resolution scale of the simulations (∼kpc). While our modelling continues to evolve MBH binaries in post-processing at smaller separations, recall that the Illustris simulations combine the two MBHs into a single remnant. Thus, after this time, we do not have accretion rates on to each MBH component, but instead on to the combined remnant. To calculate accretion rates on to each component, we use an analytic function (Kelley et al. 2019b, Equation 1) motivated by the accretion ratio ($\lambda \equiv \dot{M}_2/\dot{M}_1$) found in the 2D hydrodynamic simulations of Farris et al. (2014). The Farris et al. results find an accretion ratio that peaks near $q \sim 0.1$, and then decreases again at smaller mass ratios. Duffell et al. (2020) present an updated calculation that instead finds a monotonic relation: $\lambda \approx (0.1 + 0.9q)^{-1}$, for simulations with $q \gtrsim 0.02$. Theoretical expectations and the results of planet-star studies, however, suggest that in the limit of $q \to 0$ the ratio $\lambda \to 0$ (e.g. D'Angelo, Kley & Henning 2003). For this reason, we continue to consider the peaked model that includes a power-law decline at small q. Note that the exact location and shape of the turnover is uncertain, and might not be well captured by the Kelley et al. (2019b) fitting function.

The Illustris accretion rates are limited to Eddington. We do not enforce this criteria on each component MBH, and thus, as λ is often greater than 1, the secondary is allowed to be super-Eddington. We use the exact same treatment of the disc in the super-Eddington case as in sub-Eddington accretion.

2.3 Gravitational lensing

To calculate lensing light curves, we use the gravitational lensing models described in D'Orazio & Di Stefano (2018). In the point-source and weak-field limit, the lensing magnification is

$$\mathcal{M} = \frac{u^2 + 2}{u\,(u^2 + 4)^{1/2}}, \qquad (4)$$

for a projected separation $u = \mathrm{Re}(u_1 + u_2)$, in units of the Einstein radius. The (complex) projected separation of each component of the binary i,

$$u_i = \left[\frac{a\,c^2(\cos^2\phi_i + \sin^2 I_{\mathrm{orb}}\cos^2\phi_i)}{4G(M - m_i)\cos I_{\mathrm{orb}}\sin\phi_i}\right]^{1/2}, \qquad (5)$$

for an orbital inclination relative to the line-of-sight I_{orb} (such that $I_{\mathrm{orb}} = 0$ is an edge-on orbit), orbital phase of each component ϕ_i (thus $\phi_1 \equiv \phi_2 \pm \pi$), speed of light c, and gravitational constant G.

---

[6]In the GW-driven regime, for example, $N \propto \tau \propto a^4$.

The combined binary mass $M = m_1 + m_2$. We define the phase such that $\phi_i = \pi/2$ corresponds to component i being directly between the observer and its companion. The Einstein radius of each component is

$$R_{E,i} = (2a\, r_{s,i} \cos I_{orb} \sin \phi_i)^{1/2}. \tag{6}$$

Finally, the duration of the lensing event can be approximated as

$$\tau_{lens,i} = \frac{p}{\pi} \sin^{-1}\left(\frac{R_{E,j}}{a}\right), \tag{7}$$

where the subscripts i and j are used to indicate that the duration of the lensing event for one component depends on the Einstein radius of the other.

2.4 Doppler variability

The Doppler boosted flux is given by (D'Orazio, Haiman & Schiminovich 2015)

$$F'_{\nu'} = D^3 F_\nu, \tag{8}$$

where the Doppler shifted observed frequency is $\nu' = D\nu$. The Doppler factor is defined as $D = [\gamma(1 - v_o/c)]^{1/2}$, the Lorentz factor $\gamma \equiv (1 - v^2/c^2)^{-1/2}$, and the line-of-sight velocity $v_o = v \cos I_{orb} \cos \phi$. For all of our quantitative calculations, we calculate the Doppler boosted flux using the spectrum from equation (2) at the appropriately shifted frequencies. This is well approximated by the relation (Charisi et al. 2018)

$$\frac{F'_{\nu'}}{F_\nu} \approx (3 - \alpha_\nu)\frac{v_o}{c} + 1, \tag{9}$$

where α_ν is the spectral index at the frequency of interest. For frequencies corresponding to the typical blackbody temperatures in the disc, $\alpha_\nu \approx 1/3$, which is the spectral slope at the peak emission frequencies for a steady-state, optically thick, geometrically thin accretion disc (e.g. Frank, King & Raine 2002). The optical spectral index measured in observed AGN is seen to vary significantly (e.g. Charisi et al. 2018), but to be broadly consistent with 1/3, which we adopt throughout our analysis.

2.5 AGN intrinsic variability (damped random walk)

We model the intrinsic variability of AGN as a damped random walk (DRW) following MacLeod et al. (2010). In particular, the probability distribution for the light-curve magnitude a time Δt after a previous value at time t is characterized by an expectation value and variance given by (Ibid. Equation 5),

$$E[M_\nu(t + \Delta t)|M_\nu(t)] = M_\nu(t)e^{-\Delta t/\tau_{DRW}} + \langle M_\nu \rangle (1 - e^{-\Delta t/\tau_{DRW}}),$$

$$\mathrm{Var}[M_\nu(t + \Delta t)|M_\nu(t)] = \frac{1}{2}(SF_\infty)^2 (1 - e^{-2\Delta t/\tau_{DRW}}). \tag{10}$$

Here the magnitude $M_\nu(t) \propto \log_{10}(L_\nu[t])$, and has a mean value of $\langle M_\nu \rangle$, τ_{DRW} is the characteristic correlation time-scale, and SF_∞ is the structure function[7] as $\Delta t \to \infty$. In the limit of small and large time spans, the standard deviation becomes (Ibid. equation 4)[8]

$$\sigma_{DRW}(\Delta t \ll \tau_{DRW}) = SF_\infty \left(\frac{\Delta t}{\tau_{DRW}}\right)^{1/2},$$

$$\sigma_{DRW}(\Delta t \gg \tau_{DRW}) = SF_\infty\, 2^{-1/2}. \tag{11}$$

---

[7] A measure of self-similarity akin to an autocorrelation function.
[8] Note that 'σ' in equation (4) of MacLeod et al. (2010) refers specifically to what we are calling $\sigma_{DRW}(\Delta t \gg \tau_{DRW})$

Thus the power spectrum decreases for variations shorter than τ_{DRW} (i.e. 'red' at higher variation-frequencies), but approaches a constant value for longer time-scales (i.e. 'white' at lower frequencies). In this context, the most important feature of red-noise spectra is their natural tendency to produce coherent excursions from the mean at longer time-scales. These excursions can easily resemble order unity cycles of sinusoidal variations (like Doppler boosting) or one-off peaks (like lensing flares). In red-noise regimes of parameter space, multiple complete cycles, repeated flares, or external constraints are often needed to confirm signals.

MacLeod et al. (2010) provide empirical scaling relations for the DRW parameters as a function of wavelength, brightness, and MBH mass. To use these relations, we calculate i-band magnitudes with the bolometric corrections from Runnoe, Brotherton & Shang (2012). The distribution of DRW parameters calculated from our binary population are shown in Fig. A1 for reference. The interquartile range of τ_{DRW} is [31, 68] d and [0.13, 0.32] mag for SF_∞ (corresponding to [24 per cent, 60 per cent] in flux).

2.6 Detection criteria

The Illustris simulations and subsequent binary evolution yields masses m_1, m_2, redshift z, observed orbital period p, Eddington factor f_{Edd}, and orbital inclinations are randomly distributed over all solid angles. We also assume circular orbits throughout, and either orient all AGN discs to be 'aligned' with the binary orbit, or alternatively to be independently, randomly distributed over all angles in the 'misaligned' configuration.

We determine detectable systems as those matching the following criteria. The observed orbital period must be less than p_{max}, which is 5 yr in our fiducial model. Longer orbital periods are considered later (Section 3.4), but in general we assume that multiple lensing flares will be needed to confirm the signal type, and thus orbital periods will need to be shorter than half the total survey duration. Our fiducial value of 5 yr is motivated by the planned 10-yr duration of VRO's LSST (Ivezić et al. 2019), and the roughly decade of observations of recent all-sky surveys such as CRTS and PTF. The total flux of the secondary accretion disc (including truncation at the Hill radius) must be above the target survey sensitivity $F_{\nu,sens}$. Additionally, the change in observed flux must exceed a threshold,

$$\frac{\Delta F_\nu}{F_\nu} > \frac{1}{S/N} + 0.05,$$

$$S/N \equiv \frac{F_\nu}{F_{\nu,sens} + F_{noise}},$$

$$F_{noise} = F_\nu \times \sigma_{DRW}(\Delta t). \tag{12}$$

The higher the signal-to-noise ratio (S/N), the smaller the detectable flux variations (e.g. Sarajedini, Gilliland & Kasm 2003; Liu et al. 2016), but we assume a maximum sensitivity to variations of 5 per cent (e.g. Graham et al. 2015). Note that due to the nature of DRW noise, the amplitude is dependent on the time-scales of interest. For lensing, $\Delta t = \tau_{lens}$, while for Doppler variations, $\Delta t = p$. In the latter case, generally $p/\tau_{DRW} \gg 1$, and the DRW noise approaches a nearly constant value (equation 11).

3 RESULTS

3.1 Typical lensing features

An example AGN light curve including lensing and Doppler boosting is shown in Fig. 1. Panel (a) shows the point-source approximation
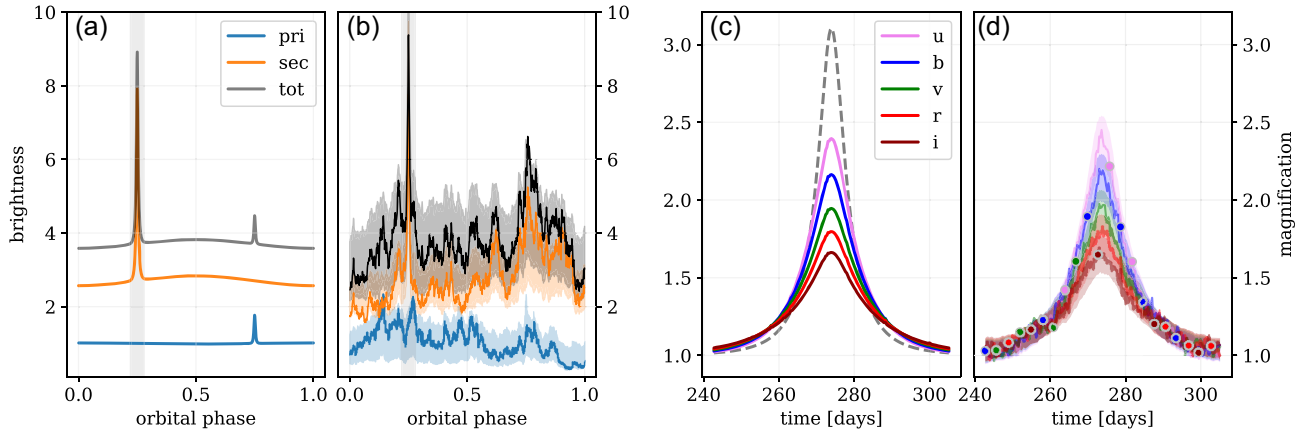
Figure 1. Lensing light curve for an example MBH binary: luminosity in arbitrary units versus time. Panel (a): point-source approximation for the primary (blue), secondary (orange), and total luminosity (black), including both lensing and Doppler boosting. The first, larger lensing peak corresponds to the secondary lensed by the primary. Panel (b): point-source light curves with added DRW variations, showing a random realization (line) and the 2σ range (shaded band). Panel (c): light curves by SDSS band using a finite-size, thin-disc emission model. The dashed black curve is the point-source approximation. Panel (d): finite-size light curves including DRW variations, with the shaded bands indicating the inter-quartile range. The solid lines show a single DRW realization applied to each band's light curve, with an additional independent 2 per cent random noise. The scatter points show time-sampling with 3-d cadence, randomly chosen across the different bands. Binary parameters: $M = 10^8\,\mathrm{M_\odot}$, $q = 0.3$, $p = 3\,\mathrm{yr}$, $z = 0.2$, $I_{\mathrm{orb}} = 0.02$, $I_{\mathrm{disc}} = 0.4\pi$, $f_{\mathrm{Edd}} = 0.25$ ($f_{\mathrm{Edd},\,2} = 0.79$). The projected closest approach of the secondary is $0.6R_{\mathrm{E,\,prim}}$.

for a bolometric light curve. The first, larger lensing peak (φ/2π = 0.25) is produced by the primary lensing the secondary, after which the secondary begins moving towards the observer as the Doppler boosting signature increases towards a maximum (φ/2π = 0.5). In this case, the peak magnification in the point-source approximation is $\mathcal{M}_2 = 3.10$ for the secondary (lensed by the primary), and $\mathcal{M}_1 = 1.85$ for the primary. In this example we choose an overall Eddington fraction for the binary, $f_{\mathrm{Edd}} = 0.25$, which gives a relative accretion rate to the secondary of $f_{\mathrm{Edd},\,2}(q = 0.3) = 0.79$. The total brightness increase at the secondary's peak is 2.41 at a closest approach of 0.3 Einstein radii, and that of the primary's is 1.21 at 0.6 Einstein radii.

The AGN light curve with the addition of typical DRW noise is shown in Fig. 1(b). Applying the DRW scaling-relations from MacLeod et al. (2010) to the secondary MBH,[9] the characteristic damping time-scale for this system is $\tau_{\mathrm{DRW}} = 77\,\mathrm{d}$ with a standard deviation at large time-scales of $\sigma_{\mathrm{DRW}} = \mathrm{SF}_\infty/\sqrt{2} = 0.12$ magnitudes, or ≈22 per cent in sensical measures of brightness. The first lensing peak is clearly distinguishable above the noise, while the second (the lensing of the primary by the secondary) is completely washed out. Note that for very small angular separations, the ratio of peak lensing magnifications $\mathcal{M}_2/\mathcal{M}_1 \approx q^{-1/2}$, and further that the accretion partition functions tend to have the secondary significantly brighter than the primary. For these reasons, the remainder of our analysis considers the detectability of only the secondary MBH's accretion disc being lensed by the primary.

Panels (a) and (b) of Fig. 1 both use the point-source approximation applied to bolometric luminosities. Panels (c) and (d) include finite-size effects and compare the brightness between different SDSS bands. Panel (c) is idealized while panel (d) includes DRW noise using the same parameters as in (b), but now applied to each band. The analytic point-source magnification for the secondary is 3.1, but when considering the finite-size leads to magnifications between 1.66 in the i band and 2.39 in the u band. In general, bluer bands are

magnified more than redder bands, even when the projected closest-approach of the lens occurs well outside of where most of the bluer emission is being produced. While the highest magnification may occur at larger (redder) radii, the typical magnification will be higher in the blue bands that are produced in more compact regions. The colour effects across the population are discussed further below.

In panel (d) of Fig. 1, an example multiband time-sampling is also marked with dots. 'Observations' are chosen in a single random band, at an interval of every 3 d. The overall cadence is consistent with preliminary expectations for the LSST survey, but the detailed survey parameters are yet to be determined (Bianco et al. 2021). For reference, the analytic duration for this event (equation 7) is 11 d, while the point-source full width at half-maximum is 8.1 d, and that of the finite-size curves (neglecting noise) ranges from 13 d in the u band to 18 d in the i band.

3.2 Detection rates and populations

Binary self-lensing detection rates are shown as a function of survey parameters in Fig. 2. We show the all-sky number of detectable sources both for lensing signals alone (blue) and cases where both the lensing and Doppler signals are detectable (orange). Generally, we assume that a survey will need to see multiple, periodic lensing flares to confirm that it is not a flare due to intrinsic variability, or a transient (i.e. one-off) lensing event. For high magnification and long-duration events, this will be a conservative assumption. For a survey with a 10-yr duration, requiring two events implies a maximum orbital period of 5 yr, which we adopt for our fiducial parameters. Typical all-sky detection rates for LSST sensitivity are 60^{+17}_{-13} (450^{+29}_{-40}) lensing, and 26^{+11}_{-9} (130^{+22}_{-27}) with Doppler, for the aligned (misaligned) configuration. Note that LSST is expected to cover roughly 1/4 of the sky (Ivezić et al. 2019). The included uncertainties are at the 2σ level based on detections from 100 realizations of our binary populations, which accounts for Poisson-like variations in the distributions of binary properties, but does not account for uncertainties in model parameters. Note that we use the point-source approximation when calculating detection rates,

---

[9] The full distribution of DRW parameters for each simulated binary's secondary MBH are plotted in Fig. A1.
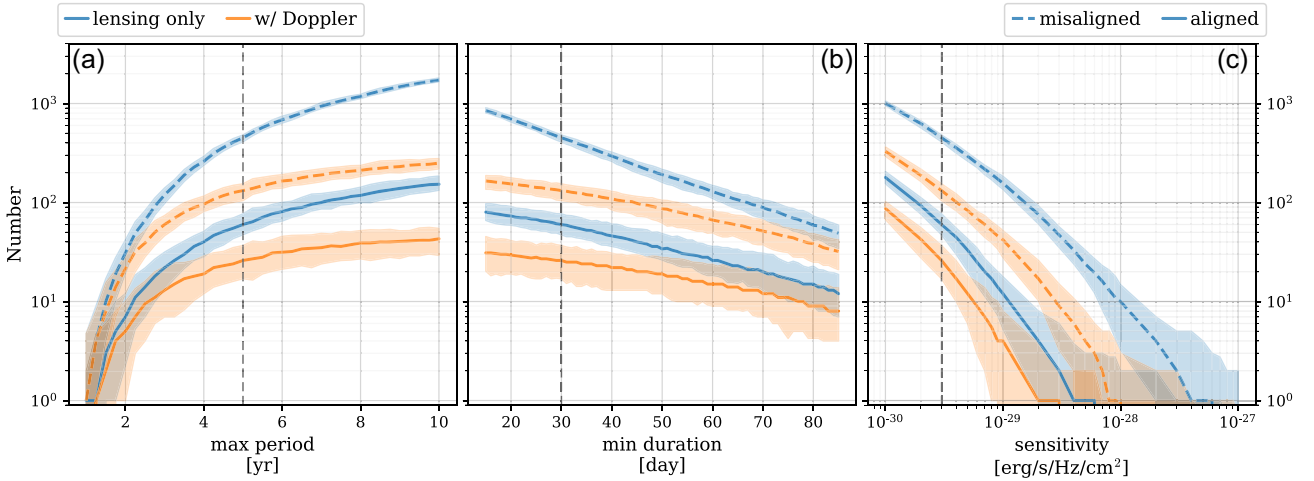
Figure 2. Detectable systems for varying survey sensitivities: the number of binaries with detectable lensing signatures (blue) and detectable lensing and Doppler variations (orange). Lines show median values while shaded regions are 2σ contours. Each panel varies one parameter while keeping the other two fixed, where the fiducial values are as follows: observed orbital periods $p_{obs} < 5$ yr, lensing signal durations $\tau > 50$ d, and R-band fluxes $F_\nu > 3.0 \times 10^{-30}$ erg s^{-1} cm^{-2} Hz^{-1}. When secondary MBH circum-single discs are perfectly aligned with the binary orbital plane (solid lines), sources are up to an order of magnitude less common than if the secondary discs are randomly oriented (dashed).

but explore finite-size effects in Section 3.3, and find that they are unlikely to produce a noticeable change on the overall event rates.

Because the binary hardening time-scale, and thus the number of binaries at a given orbital period, depends strongly on the orbital period ($N \propto p^{8/3}$), the resulting detection rate is quite sensitive to the maximum detectable orbital period. If the fiducial maximum orbital period decreases by a factor of 2 ($p < 2.5$ yr), the all-sky numbers drop to 14^{+8}_{-7} (66^{+17}_{-15}) lensing, and $9.5^{+6.5}_{-5.5}$ (39^{+13}_{-11}) with Doppler. The lensing population more closely follows the overall period-distribution of binaries than the Doppler population, because the Doppler detectability increases for smaller (faster) orbits.

Lensing flare durations and the DRW damping time-scales are both typically 30–100 d in duration. However, including DRW noise only has a moderate effect on lensing detection rates. Setting $F_{noise} = 0$ in equation (12) (compare 'white' versus 'DRW' in Table A1) increases the detection rate from a fiducial value of 60^{+17}_{-13} (450^{+29}_{-40}) to 73^{+16}_{-13} (510^{+31}_{-44}) for the aligned (misaligned) configuration. The change in Doppler (alone) detection rates, however, is almost a factor of 2, from 160^{+23}_{-20} (370^{+36}_{-32}) to 220^{+31}_{-18} (670^{+51}_{-38}). The difference is that Doppler boosts typically have magnitudes on the order of tens of percent while lensing magnifications are typically order unity. The effect on the combined detection rate changes from 26^{+11}_{-9} (130^{+22}_{-27}) to 44^{+15}_{-10} (250^{+32}_{-26}). Lensing signatures may be more robust against DRW noise compared to Doppler variability, but this would need to be confirmed using a realistic detection pipeline.

We assume that some minimum number of detections spanning the lensing event are required to properly characterize it. In Fig. 2(b), we parametrize this criterion in terms of the minimum lensing event duration that the survey is sensitive to. In practice, this is the number of intra-flare photometric measurements required for detection, multiplied by the survey cadence. As a fiducial value, we assume 10 intra-flare measurements are required with a cadence of 3 d (roughly that expected for LSST; Ivezić et al. 2019), yielding a minimum duration of 30 d. If this value is halved to only 15 d, the all-sky number of events is 80^{+17}_{-14} (850^{+58}_{-43}) lensing, and 31^{+14}_{-11} (160^{+22}_{-29}) with Doppler. Fig. 2(c) shows the detection rate dependence on r-band

survey sensitivity. The fiducial value of 3×10^{-30} erg s^{-1} cm^{-2} Hz^{-1} is motivated by the expectation for LSST. If this can be boosted to 2×10^{-30} erg s^{-1} cm^{-2} Hz^{-1} detections increase proportionally to 93^{+19}_{-16} (630^{+42}_{-58}) lensing, 42^{+13}_{-15} (190^{+29}_{-24}) with Doppler. An order of magnitude decrease in sensitivity, however, comparable to the sensitivity of SDSS, yields all-sky numbers of $2.0^{+4.0}_{-2.0}$ (47^{+10}_{-12}) lensing, $1.0^{+1.0}_{-1.0}$ ($9.0^{+6.0}_{-5.7}$) with Doppler. Unless most secondary AGN discs are misaligned with their binary orbits, SDSS-like sensitivities are thus unlikely to detect MBHB lensing signatures.

The parameters of simulated MBH binaries with detectable lensing signatures are plotted in Fig. A2 for both the 'aligned' (green) and 'misaligned' (orange) configurations. In the aligned case, the median and interquartile range of lensing detectable systems are: $M = 1.1^{+1.3}_{-0.6} \times 10^9$ M$_\odot$, $q = 1.2^{+5.6}_{-0.8} \times 10^{-2}$, $p = 3.4^{+0.8}_{-0.9}$ yr, and $z = 0.46^{+0.24}_{-0.20}$. Lensing detectable systems pick out higher masses and more extreme mass-ratios than the overall population. For a given orbital separation, higher masses and more extreme mass-ratios lead to higher lensing probabilities as a larger range of inclination angles will produce equivalent magnifications.[10] The trend is further bolstered by larger masses and more extreme mass ratios producing more luminous secondaries (see Section 2.2). The correlation between Eddington factor and redshift, and anticorrelation with mass are produced by the same selection effect. In the misaligned geometry, the median and interquartile values are: $M = 4.4^{+7.5}_{-2.0} \times 10^8$ M$_\odot$, $q = 3.5^{+7.9}_{-2.7} \times 10^{-2}$, $p = 3.7^{+0.6}_{-0.8}$ yr, and $z = 0.75^{+0.44}_{-0.26}$. The changes relative to the aligned case, particularly lower masses, larger (more-moderate) mass-ratios, and higher redshifts are all driven by the misaligned discs presenting larger angular areas and thus being brighter than for aligned discs.

Fig. A2 also shows the observed signal properties for aligned and misaligned models. For a lensing signal to be detectable, the binary orbit must be nearly edge-on ($I_{orb} \approx 0$). In the aligned configuration,

---

[10]Note that Doppler signatures are also more detectable in the same population of systems due to higher orbital velocities (see fig. 10 of Kelley et al. 2019b).
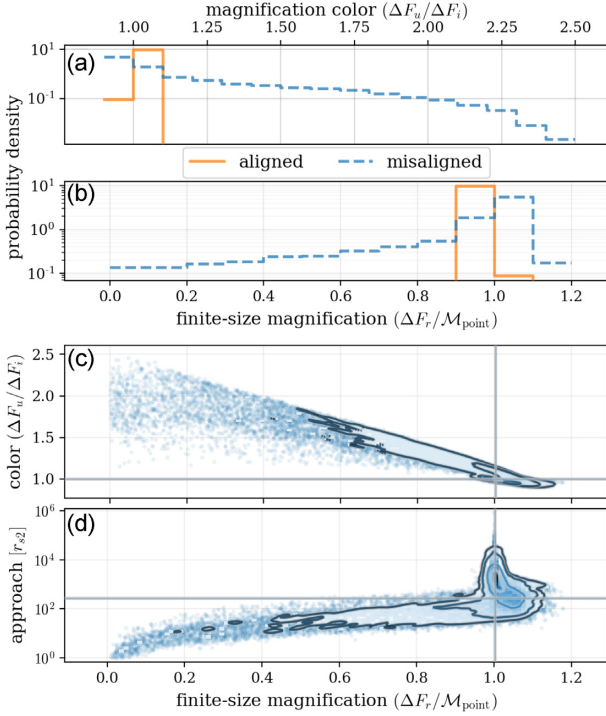
Figure 3. Distribution of magnification colours, and magnification amplitudes relative to the point-source approximation. Panel (a) plots 'colour', defined as the ratio of magnifications in the u-band relative to the *i* band. Panel (b) shows the *r*-band magnification relative to the point-source approximation, and panel (c) shows the strong anticorrelation of this ratio versus magnification colour. Panel (d) plots closest approach (in units of secondary Schwarzschild radii) relative to finite-size magnification. In panels (c) and (d), only misaligned systems are plotted because magnification and colour are almost identically unity for aligned systems. These distributions are shown for 100 realizations of detected systems, roughly 3000 (29 000) for aligned (misaligned) geometries.

the secondary AGN disc orientation is by definition the same ($I_{disc} \equiv I_{orb}$), while in the misaligned case it is oriented randomly. In the aligned configuration, however, as $I_{disc} \to 0$ the flux from the AGN decreases as $F_\nu \propto I_{disc}$ as a smaller and smaller angular area of the disc remains visible. This effect could be significantly enhanced if high optical-depth obscuring torii are present in MBHBs as they are in single AGN (see, e.g. Ueda et al. 2014). This important issue is discussed further in Section 4. The resulting effect is that in the aligned case, I_{orb} tends to be larger than in the misaligned case: $I_{orb} = 9.5^{+4.7}_{-3.5} \times 10^{-2} \approx 5°$ versus $I_{orb} = 4.8^{+3.5}_{-2.4} \times 10^{-2} \approx 3°$. This leads to a proportional change in typical lensing magnifications: $1.9^{+0.5}_{-0.4}$ (aligned) versus $2.5^{+1.5}_{-0.7}$ (misaligned). Lensing durations are very similar in both geometries: 56^{+24}_{-15} (aligned) and 46^{+18}_{-9} d (misaligned).[11]

3.3 Finite-size effects and chromatic lensing

The top panel (a) of Fig. 3 shows the ratio of magnification in the *u* band to that of the *i* band. Larger values correspond to AGNs appearing bluer at the lensing peak. For the aligned configuration, lensing is almost perfectly achromatic: The *u*-band magnification is

---

[11]Note that in equation (7), we do not explicitly account for inclination dependence that is small for $I_{orb} \approx 0$ (see equation 5 of Wiktorowicz et al. 2021).

---

within 2 per cent that of the *i* band in the interquartile range. For aligned systems, the AGN disc is nearly edge-on, and the lensing magnification affects all disc radii (and thus colours) similarly. For misaligned configurations, most systems are still nearly achromatic with the median and interquartile range: $\Delta F_u / \Delta F_i = 1.00^{+0.19}_{-0.02}$, but 10 per cent of systems have $\Delta F_u / \Delta F_i > 1.56$. Half of lensing-detectable systems are redder at the lensing peak, though only by a small amount: $\Delta F_u / \Delta F_i = 0.98^{+0.01}_{-0.02}$. This occurs in binaries where the peak emission radii of the redder bands are comparable to (i) the Hill radius of the secondary MBH, and also (ii) near the projected separation of the lens at closest approach. In these cases, the secondary MBH's accretion disc is truncated, and the unmagnified emission is attenuated in the redder bands. During lensing, the bluer bands are still brighter, but the relative increase is more substantial in the redder bands.

Panel (b) of Fig. 3 shows the disc magnification in the *r* band compared to the magnification in the point-source approximation. For aligned systems, the magnification is almost identical to the point-source approximation: In situations where detectable lensing occurs, the angular area of the nearly edge-on disc tends to be small, and different radii are projected to similar angular offsets. For misaligned binaries, the majority of systems are clustered around the point source approximation: $1.00^{+0.03}_{-0.08}$. Out of the misaligned systems, 58 per cent are magnified more than in the point-source approximation, but only slightly: the highest excesses reaching $F_r^{lensed} / F_r^{lensed,point} \approx 1.10$. These are the same binaries that result in lensing peaks that are reddened (as opposed to the more common blue peaks). Both phenomena are caused by lensing of the disc just within the truncation radius that overcompensates for attenuation in the unlensed-case. This can be seen in panel (c) of Fig. 3, which shows the strong anticorrelation between lensing colour and magnification relative to the point-source approximation.

To understand these reddened systems more carefully, consider the (projected) passage of the lensing primary across the plane of the secondary's accretion disc. Take the projected closest approach of the primary to be just outside of the characteristic radius for *r*-band emission. If the secondary disc extends to infinity (i.e. it is not truncated), then the bluer emission comes from a more compact region that is lensed more strongly – even though the lens (primary) is closer to the *r*-band radius at one azimuth in the disc, the average projected distance to the bluer emitting regions is still smaller than the average distance to the *r*-band emitting regions. For the infinite disc, there is a larger amount of *r*-band emitting material at larger radii (including on the opposite side of the disc) that is farther from the lens and magnified less. If the secondary disc is instead truncated just beyond the closest approach radius (and the characteristic *r*-band radius), then there is no longer as much *r*-band emitting material at larger radii, and the relative magnification of the *r*-band emission is much higher. Note that these reddened systems are still magnified less than in the case of the point-source approximation applied to an untruncated AGN disc.

A noticeable tail in the population extends towards smaller magnifications with 10 per cent of systems having $F_r^{lensed} / F_r^{lensed,point} < 0.56$. Smaller than point-source magnifications are caused by systems in which the minimum angular separation is very small, and the point-source approximation begins to diverge (equation 4). In actuality, only a small fraction of the AGN disc passes at these close separations to the lens, and only that fraction of the emission is magnified to high levels. The correlation between closest projected approach distance at peak magnification and the finite-size magnification is shown in panel (d) of Fig. 3. The point-source approximation is breaking down right when the closest approach is comparable and smaller than

the peak emission radii of interest ($\sim 100 r_s$).[12] Note that the point-source calculation is quite accurate for all but the smallest angular separations, which are far less common. Our calculated detection rates, which use the point-source approximation, are thus unlikely to be significantly effected by finite-size effects, although they might slightly change the distribution of detected binary parameters and the differences between aligned and misaligned systems (see Fig. A2).

An upper-bound to the wavelength-dependent maximum magnification can be calculated by setting the minimum angular separation to be the extent of the AGN disc at a given emitting wavelength, i.e. $u_{\min} = \max[u_{\mathrm{orbit}}, u_{\mathrm{disc}}]$. Using the radius of peak emission for a given frequency-band (here we have normalized to the SDSS r band),

$$r_{\mathrm{peak}}(\nu) = 16.0\, r_{s,i}\; f_{\mathrm{Edd},i}^{1/3} \left(\frac{m_i}{10^8\,\mathrm{M_\odot}}\right)^{-1/3} \left(\frac{\nu}{4.6\times 10^{14}\,\mathrm{Hz}}\right)^{-4/3},$$
(13)

and approximating the magnification as $\mathcal{M} \approx 1/u$,

$$\mathcal{M}_{\mathrm{peak}}^{\max} = 7.25 \left(\frac{\nu}{4.6\times 10^{14}\,\mathrm{Hz}}\right)^{4/3} \left(\frac{p}{3\,\mathrm{yr}}\right)^{1/3} \left(\frac{q}{0.1}\right)^{-2/3}$$
$$\times \frac{(1+q)^{1/6}}{f_{\mathrm{Edd},2}^{1/3}}.$$
(14)

In practice, the true peak magnification will be lower after convolving the full magnification field with the disc surface brightness. The maximum magnification at any wavelength can be estimated by considering the magnification of emission emanating from the ISCO of the source BH (D'Orazio & Di Stefano 2020):

$$\mathcal{M}^{\max} = \frac{R_{E,1}}{3\, r_{s,2}} \approx \frac{(2\, a\, r_{s,1})^{1/2}}{3\, r_{s,2}} \approx 7 \left(\frac{a}{100\, R_s}\right)^{1/2} \frac{\sqrt{1+q}/q}{\sqrt{2}}$$
$$\sim 100 \left(\frac{p}{3\,\mathrm{yr}}\right)^{1/3} \left(\frac{M}{10^8\,\mathrm{M_\odot}}\right)^{-1/3} \left(\frac{q}{0.1}\right)^{-1} (1+q)^{1/2}, \quad (15)$$

where $R_s = 2GM/c^2$, and the top line assumes a conservative $q = 1$.

Note that these results will depend on accretion disc structure. In this analysis, we assume a Shakura–Sunyaev thermal structure, but observed lensing systems will be able to serve as probes of this assumption.

3.4 Long-period, long-duration signals

Our fiducial models and detection rates (i.e. Table A1) assume that multiple, periodically repeating flares must be identified to confirm a self-lensing binary origin. One can imagine, however, that high S/N events and long-duration events where the lensing light curve can be thoroughly sampled, could allow identification of a self-lensing binary with only one event. Such an event would then offer a prediction for the arrival of the next lensing flare (e.g. Hu et al. 2020). Fig. 4 shows the number of detectable lensing-binaries without requiring multiple events to be detectable. In this case, we require lensing durations to be longer than 30 d, and use the same (S/N-dependent) detection criteria as before (equation 12). The total binary population shows two regimes. At periods shorter than $\approx 10^2$ yr, binaries are firmly in the GW driven regime and spend less and less time at smaller separations and thus, as a population, there are ever fewer. At longer orbital periods ($\gtrsim 10^2$ yr),
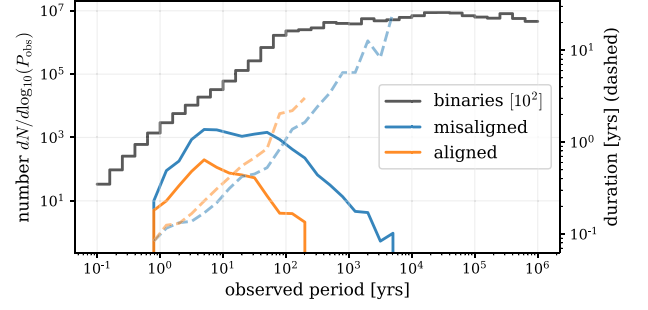
[12]See also the discussion of finite-sized effects in (D'Orazio & Di Stefano 2018).

Figure 4. Occurrence rate of long-period lensing binaries. Solid lines (left-hand axis) show the number of all simulated binaries (black; shifted by 10^2), and the number of lensing-detectable binaries in the misaligned (blue) and aligned (orange) configurations. Dashed lines (right-hand axis) show the average lensing duration at each observed orbital period. We require lensing durations $\tau_{\mathrm{lens}} > 30$ d, and assume an LSST-like sensitivity of 3×10^{-30} erg s^{-1} cm^{-2} Hz^{-1}, but no longer impose a maximum orbital period (to ensure multiple detectable events). We assume a 5-yr observing duration both for calculating S/N (at short periods) and also the probability of the lensing event occurring during the observing window (at long periods).

binary hardening rates are determined largely by interactions with their local environment, primarily in the form of stellar scattering and torques from a circumbinary disc, which end up producing more uniform hardening rates versus separation (see, e.g. Kelley et al. 2017a).

The distribution of lensing-detectable binaries cuts off sharply both at short and long orbital periods. At short periods, the duration of lensing events becomes small, and even the high cadence of an LSST-like survey becomes unlikely to make enough observations during the lensing event to properly characterize it as such. This effect impacts both aligned and misaligned systems in the same way. At long periods, lensing signals are competing with the saturated levels of intrinsic red-noise (recall, modelled as a DRW; see equation 11). At the same time, even though the maximum possible lensing magnification goes up for larger binary separations (equation 15), randomly oriented orbital inclinations lead to typically larger source-lens angular separations, and thus typically smaller lensing magnifications. Thus, at long orbital periods, lensing events are drowned-out by noise. This happens more easily for the aligned geometry, in which the secondary AGN tend to be fainter, yield lower S/Ns, and thus require larger magnifications to be observed above the noise (see equation 12). In our simulated populations, lensing signals become undetectable above $p \approx 200$ yr for aligned binaries, and $\approx 10^4$ yr for misaligned systems. The decline in number of detectable systems at large periods is only contributed to by the decreasing probability of the lensing event occurring during the observing window.

The overall number of long-period lensing binaries will far outnumber those with periods of a few years that allow for multiple events to be observed in $\sim$decade-long surveys. The duration of these lensing events, proportional to the orbital period, will be months to a few years in duration. Most of these systems will have low lensing magnifications, but as long as the DRW model remains applicable (which we assume in Fig. 4), the intrinsic noise will be white in character, possibly making lensing flares more distinguishable. At the same time, as this regime of long-duration AGN variability is only now being explored with precision photometry, additional confusion sources (e.g. [partial-]tidal disruption events, changing-look/changing-character AGN, etc.).

4 DISCUSSION

There are no confirmed examples of sub-pc MBH binaries, and many uncertainties regarding both their formation (e.g. the rate and parametric distributions of MBHs in galaxy mergers) and particularly their binary evolution (e.g. stellar scattering efficiencies, local gas densities, etc.). The overall predicted occurrence rates of luminous close-binaries has systematic uncertainties that are likely at least a factor of a few. Additionally, the binary merger physics is particularly challenging to model in extreme mass-ratio binaries, which represent a noticeable fraction of the target self-lensing population. In this analysis, we have used the geometrical optics approximation, which neglects strong lensing effects, in addition to ignoring occultation of the source disc by the lens MBH and any optically thick disc around it. A recent analysis by Ingram et al. (2021) for X-ray self-lensing shows that even partial-eclipse can significantly alter the lensing morphology. The more extended optical emission will be less effected by occultation, but it will still be an important effect when analysing (candidate) detections and performing parameter inference. However, we do not expect occultation to significantly change expected detection rates. These effects are most important in the less common strong-lensing events, and when eclipses or partial eclipses occur, the overall change in flux can still be significant (Ingram et al. 2021) and thus likely detectable.

If the signal observed in recent pulsar timing array data (Arzoumanian et al. 2020b) is confirmed to be an astrophysical GW background, expected to be determined within the next couple of years (Pol et al. 2021), it would definitively demonstrate the existence of a cosmological population of MBHBs. Our populations of MBHBs derived from Illustris produce GW amplitudes roughly a factor of $\approx$2–3 lower than the prospective GW signal. If the GW signal is confirmed, this would suggest broad agreement and perhaps a higher occurrence rate of sources. Note, however, that extreme mass-ratio binaries contribute very little to the background (e.g. Kelley et al. 2018), and also that numerous parameters in binary populations and evolution contribute to the GW background amplitude (e.g. Middleton et al. 2021). Nearby and particularly-massive MBHBs detected through self-lensing would be promising candidates for targeted GW searches (e.g. Arzoumanian et al. 2020a), and the identification of multimessenger sources presents exciting opportunities for novel scientific studies (e.g. Kelley et al. 2019a).

Based on our models, we predict that the Vera Rubin Observatory's LSST survey should detect ~10–100 of self-lensing MBHB systems (see Table A1). The uncertain distribution of alignment angles, between binary orbital planes and those of the secondary accretion discs, leads to a difference in detection rate of about a factor of 7. For lensing signals to be detectable, the orbital plane needs to be viewed nearly edge-on by the observer to produce sufficiently small angular separations between source and lens. If the secondary AGN disc is aligned with the orbit, it also presents a smaller projected area and thus much lower flux, making fewer systems detectable. The relative orientation of the secondary disc also has a significant impact on the distribution of lensing magnifications, and the relative brightness of different photometric bands. This suggests that orientations can be measured from a lensing population, the degeneracy between detection rates and disc alignment distributions can be broken, and constraints can be made on the overall occurrence rate of close-separation MBHBs. With the total binary mass also measurable from the orbital period, the binary orbital parameters (including individual masses, eccentricity, argument of pericentre, separation, and inclination) of self-lensing MBHBs can be very well constrained (see Hu et al. 2020). Because these types of systems will also tend to have at least millions of years before their eventual coalescence, they will be long-term laboratories for studying the accretion and dynamics of binaries.

The other most-promising indicators of AGN in binary systems are likely periodic photometric variability (Graham et al. 2015; Charisi et al. 2016; Liu et al. 2019; Chen et al. 2020), or time-variable/kinematically-offset broad emission lines (e.g. Eracleous et al. 2012; Runnoe et al. 2017). There are significant challenges to both methods, particularly due to contamination from noise sources in single AGN (e.g. Vaughan et al. 2016; Liu, Gezari & Miller 2018; Kelley 2021b). The DRW red-noise that is characteristic of AGN is particularly challenging to distinguish from long-duration periodic signatures. Accounting for DRW noise in our models decreases the number of binaries with detectable Doppler variable lightcurves by roughly a factor of four (see Table A1). Lensing flares, however, tend to have much larger amplitudes, and our models show an only mild decrease ($\approx$15 per cent) in detection rate when including red noise. We predict that both lensing flares and Doppler variations should be simultaneously detectable for a few to tens of binaries with LSST.

The Vera Rubin Observatory's LSST is extremely promising for AGN binary observations. According to our population models, current surveys do not have sufficient depth and coverage to plausibly expect detections. Using simple parametrizations for Pan-STARRS (Liu et al. 2019), PTF (Charisi et al. 2016), *Kepler* (Koch et al. 2010), and *Gaia*,[13] we find zero detections within the 2σ range; while for CRTS (Graham et al. 2015) and ZTF Bellm et al. (2019), the median plus 2σ detection rate is roughly one source after 5 yr of data. The survey parameters and resulting detection rates are shown in Table A2. It is worth noting that the best candidate for a lensing MBH binary was detected by *Kepler* as KIC 11606854 ('Spikey'; Hu et al. 2020; Kun, Frey & Gabányi 2020). This source shows a very short (~10 d) flare, that is well resolved and clearly above the noise. Our models firmly predict that no lensed AGN should have been observable in the *Kepler* field, owing to the rarity of MBHBs and *Kepler*'s small field of view. Indeed, Spikey is one of only dozens of AGN in the *Kepler* field (Smith et al. 2018), implying an extremely fortuitous event, a very high event rate, or an alternative source model. If Spikey is confirmed to be a self-lensing MBHB, a detection rate of $\gtrsim$10^{-2} would be very difficult to explain with our Illustris-based MBHB populations.

In general, bluer optical bands show higher lensing magnifications because their compact emitting regions are more uniformly magnified. However, because AGN and particularly post galaxy-merger galactic nuclei tend to have high column densities (Koss et al. 2016; Ricci et al. 2017; Koss et al. 2018), bluer near-optical observing bands may often be partially or entirely obscured. The columns and obscuration fractions of AGN are believed to increase significantly for observers viewing AGN discs edge-on (e.g. Ramos Almeida & Ricci 2017). If circumbinary discs tend to be aligned with binary orbits, and if these dusty torii are still present in close binaries, this could present a significant challenge to observing self-lensing signatures. Such obscuring regions, however, may offer a different way to find reprocessed lensing and Doppler boost signatures in the IR (D'Orazio & Haiman 2017). Alternatively, dusty torii that tend to be perpendicular to the binary orbital plane, as can occur for eccentric orbits (e.g. Martin & Lubow 2017), would produce much lower obscuring fractions.

Both theory (e.g. Netzer & Laor 1993; Nenkova et al. 2008) and observations (e.g. Suganuma et al. 2006; Koshida et al. 2014) give typi-

---

[13]https://www.cosmos.esa.int/web/gaia.

cal radii of the dusty torus to be $R_{dust} \approx 0.1$ pc $\left(L_\nu/10^{45} \text{ erg s}^{-1}\right)^{1/2}$. Applying this relation to the combined luminosity of both MBHs in our population of lensing-detectable binaries gives a median and interquartile range: $R_{dust} = 7.7^{+5.0}_{-2.8} \times 10^{-2}$ pc $= 13^{+12}_{-6} \, a_{sep}$, where a_{sep} is the binary separation. If we assume that the dusty torus is disrupted if $R_{dust}/a_{sep} < 10$ ($R_{dust}/a_{sep} < 3$), then 38 per cent (13 per cent) of lensing binaries would be unobscured even if aligned with the circumbinary disc.[14] If, on the other hand, we assume that circumbinary discs are randomly oriented and obscuration is determined by the covering fraction of torii, then we might expect ≈ 25 per cent of lensing systems to be unobscured.[15] Applying these fractions to the expected detection rates for LSST, assuming it covers 1/4 of the sky, and assuming that obscured binaries are completely undetectable, we get a very conservative estimate of ≈ 6 detectable systems if all are aligned, and ≈ 30 if all are misaligned.

5 CONCLUSIONS

In this study we have combined sophisticated populations of MBH binaries with models of AGN discs and gravitational self-lensing that will be detectable with fast-cadence all-sky surveys like VRO's LSST. Our key conclusions are as follows:

(i) We expect 10–100 self-lensing systems to be detectable with LSST in our fiducial models, even after estimating the effects of dusty-torus obscuration and including intrinsic AGN variability. Most current surveys are unlikely to have sufficient coverage to contain detectable lensing events.

(ii) Detectable lensing events have median magnifications of ~ 100 per cent, with durations of a few tens of days. Sources typically have total masses between 10^8 and $10^9 \, M_\odot$, mass-ratios 10^{-2}–10^{-1}, and orbital periods of multiple years.

(iii) Because lensing events are intrinsically rare, surveys with a given depth should attempt to cover as large an area of the sky as possible with a cadence of 3–7 d. Lensing events can be chromatic for some configurations, brightening more in bluer bands, but those bands may also be subject to additional obscuration.

(iv) Detectable lensing signatures require viewing angles near the orbital plane. A key uncertainty in our models is whether the secondary accretion disc tends to be aligned with the orbit, and thus typically also edge-on, or may be misaligned and randomly oriented.

(v) Magnifications tend to be nearly achromatic, but differences between observing bands can strongly probe the AGN disc inclination and structure. Peak magnifications tend to closely match the point-source approximation, with detectable deviations only in misaligned geometries.

(vi) We find that intrinsic DRW red-noise in AGN does not significantly inhibit lensing detections, but does make coincident Doppler variations much more difficult. Doppler signals should be detectable in $\approx 1/3$ of lensing binaries.

(vii) Our fiducial detection models require short enough orbital periods to observe multiple, periodic lensing flares. There should, however, be orders of magnitude more lensing binaries at much longer orbital periods (tens to thousands of years) having flares that last months to years.

(viii) Our calculations use the geometrical optics approximation, and do not account for occultation and eclipse that have been shown by Ingram et al. (2021) to noticeably impact the lensing flare shape, particularly for strong-lensing events in misaligned geometries. We do not expect occultation or strong lensing to significantly affect detection rates, the focus of this analysis, but they will be important for analysing detections and particularly for parameter inference.

The modelling of MBH binary populations includes numerous significant uncertainties, both regarding their rates of formation and the complex physics of their binary evolution. Our understanding of MBH binaries interacting with circumbinary accretion flows has rapidly progressed in the last decade, but remains very challenging to probe with detailed simulations. The efficiency of driving material to accrete on to each component MBH is particularly important for predicting and understanding the resulting electromagnetic signatures. Further modelling of circumbinary accretion is thus particularly important, especially including effects such as AGN feedback and complex geometries.

The confident detection of self-lensing in an AGN presents many exciting opportunities. Foremost, it would be the first confirmed detection of a gravitationally-bound MBH binary. Measurement of the orbital period and lensing characteristics can strongly constrain the MBH components, their accretion, and their orbital parameters. As no MBHBs have yet been observationally confirmed, binary populations remain uncertain. The detection of an ensemble of self-lensing systems could place tight constraints on MBH binary formation and evolution. In exceptional systems with high S/Ns and small impact parameters, lensing events could be used to probe the inner structure of AGN accretion discs. Nearby and high mass-ratio systems could also be promising multimessenger sources combined with low-frequency GWs that are expected to be detected within the next few years.

---

[14]Note that these particular values (10 and 3) are arbitrarily chosen.
[15]Estimated using the obscuration/Type-2 fraction of AGN from Hasinger (2008), Merloni et al. (2014), Suh et al. (2019), and X-Ray bolometric corrections from Runnoe et al. (2017).

DATA AVAILABILITY

The Illustris data are available online at www.illustris-project.org (Nelson et al. 2015), and Illustris-TNG data at www.tng-project.org (Nelson et al. 2019). One realization of our full binary population is available at zenodo:4068485 (Kelley 2020).

REFERENCES

Antonucci R., 1993, ARA&A, 31, 473
Armitage P. J., Natarajan P., 2002, ApJ, 567, L9
Artymowicz P., Lubow S. H., 1994, ApJ, 421, 651
Artymowicz P., Lubow S. H., 1996, ApJ, 467, L77
Arzoumanian Z. et al., 2020a, ApJ, 900, 102
Arzoumanian Z. et al., 2020b, ApJ, 905, L34
Astropy Collaboration et al., 2013, A&A, 558, A33
Bardeen J. M., Petterson J. A., 1975, ApJ, 195, L65
Barr P., Mushotzky R. F., 1986, Nature, 320, 421
Barvainis R., 1987, ApJ, 320, 537
Begelman M. C., Blandford R. D., Rees M. J., 1980, Nature, 287, 307
Bellm E. C. et al., 2019, PASP, 131, 018002
Beskin G. M., Tuntsov A. V., 2002, A&A, 394, 489
Bianco F. B. et al., 2021, preprint (arXiv:2108.01683)
Binney J., Tremaine S., 1987, Galactic Dynamics. Princeton Univ. Press, Princeton, NJ
Bogdanović T., 2015, in Sopuerta C. F., ed., Astrophysics and Space Science Library, Vol. 40, Gravitational Wave Astrophysics. Springer, Berlin, p. 103
Burke-Spolaor S., 2013, Class. Quantum Gravity, 30, 224013
Chandrasekhar S., 1943, ApJ, 97, 255
Charisi M., Bartos I., Haiman Z., Price-Whelan A. M., Graham M. J., Bellm E. C., Laher R. R., Márka S., 2016, MNRAS, 463, 2145
Charisi M., Haiman Z., Schiminovich D., D'Orazio D. J., 2018, MNRAS, 476, 4617
Chen Y.-C. et al., 2020, MNRAS, 499, 2245
D'Angelo G., Kley W., Henning T., 2003, ApJ, 586, 540
D'Orazio D. J., Di Stefano R., 2018, MNRAS, 474, 2975
D'Orazio D. J., Di Stefano R., 2020, MNRAS, 491, 1506
D'Orazio D. J., Duffell P. C., 2021, ApJ, 914, L24
D'Orazio D. J., Haiman Z., 2017, MNRAS, 470, 1198
D'Orazio D. J., Haiman Z., Duffell P., MacFadyen A., Farris B., 2016, MNRAS, 459, 2379
D'Orazio D. J., Haiman Z., Schiminovich D., 2015, Nature, 525, 351
De Rosa A. et al., 2019, New Astron. Rev., 86, 101525
Detweiler S., 1979, ApJ, 234, 1100
Duffell P. C., D'Orazio D., Derdzinski A., Haiman Z., MacFadyen A., Rosen A. L., Zrake J., 2020, ApJ, 901, 25
Duffell P. C., Haiman Z., MacFadyen A. I., D'Orazio D. J., Farris B. D., 2014, ApJ, 792, L10
Eggleton P. P., 1983, ApJ, 268, 368
Eracleous M., Boroson T. A., Halpern J. P., Liu J., 2012, ApJS, 201, 23
Fanaroff B. L., Riley J. M., 1974, MNRAS, 167, 31P
Farris B. D., Duffell P., MacFadyen A. I., Haiman Z., 2014, ApJ, 783, 134
Farris B. D., Duffell P., MacFadyen A. I., Haiman Z., 2015, MNRAS, 447, L80
Fossati G., Maraschi L., Celotti A., Comastri A., Ghisellini G., 1998, MNRAS, 299, 433
Foster R. S., Backer D. C., 1990, ApJ, 361, 300
Frank J., King A., Raine D. J., 2002, Accretion Power in Astrophysics, 3rd edn, Cambridge University Press, Cambridge, UK
Genel S. et al., 2014, MNRAS, 445, 175
Gould A., Loeb A., 1992, ApJ, 396, 104
Gould A., Rix H.-W., 2000, ApJ, 532, L29
Graham M. J. et al., 2015, MNRAS, 453, 1562
Haiman Z., Kocsis B., Menou K., 2009, ApJ, 700, 1952
Hasinger G., 2008, A&A, 490, 905
Hayasaki K., Mineshige S., Sudou H., 2007, PASJ, 59, 427
Hellings R. W., Downs G. S., 1983, ApJ, 265, L39
Hook I. M., McMahon R. G., Boyle B. J., Irwin M. J., 1994, MNRAS, 268, 305
Hu B. X., D'Orazio D. J., Haiman Z., Smith K. L., Snios B., Charisi M., Di Stefano R., 2020, MNRAS, 495, 4061
Hunter J. D., 2007, Comput. Sci. Eng., 9, 90
Ingram A., Motta S. E., Aigrain S., Karastergiou A., 2021, MNRAS, 503, 1703

Ivezić Ž. et al., 2019, ApJ, 873, 111
Jaffe A. H., Backer D. C., 2003, ApJ, 583, 616
Kelley L. et al., 2019a, BAAS, 51, 490
Kelley L. Z., 2020, Zenodo
Kelley L. Z., 2021b, MNRAS, 500, 4065
Kelley L. Z., Blecha L., Hernquist L., 2017a, MNRAS, 464, 3131
Kelley L. Z., Blecha L., Hernquist L., Sesana A., Taylor S. R., 2017b, MNRAS, 471, 4508
Kelley L. Z., Blecha L., Hernquist L., Sesana A., Taylor S. R., 2018, MNRAS, 477, 964
Kelley L. Z., Haiman Z., Sesana A., Hernquist L., 2019b, MNRAS, 485, 1579
Kelley L., 2021a, J. Open Source Softw., 6, 2784
Kelly B. C., Bechtold J., Siemiginowska A., 2009, ApJ, 698, 895
Khan F. M., Just A., Merritt D., 2011, ApJ, 732, 89
Kluyver T. et al., 2016, Positioning and Power in Academic Publishing: Players, Agents and Agendas. IOS Press, Amsterdam, Netherlands
Koch D. G. et al., 2010, ApJ, 713, L79
Koshida S. et al., 2014, ApJ, 788, 159
Koss M. J. et al., 2016, ApJ, 825, 85
Koss M. J. et al., 2018, Nature, 563, 214
Kun E., Frey S., Gabányi K. É., 2020, MNRAS, 496, 3336
Liska M., Tchekhovskoy A., Ingram A., van der Klis M., 2019, MNRAS, 487, 550
Liu T. et al., 2016, ApJ, 833, 6
Liu T. et al., 2019, ApJ, 884, 36
Liu T., Gezari S., Miller M. C., 2018, ApJ, 859, L12
MacLeod C. L. et al., 2010, ApJ, 721, 1014
Maeder A., 1973, A&A, 26, 215
Magorrian J., Tremaine S., 1999, MNRAS, 309, 447
Mao S., Paczynski B., 1991, ApJ, 374, L37
Martin R. G., Lubow S. H., 2017, ApJ, 835, L28
Merloni A. et al., 2014, MNRAS, 437, 3550
Merritt D., 2013, Class. Quantum Gravity, 30, 244005
Middleton H., Sesana A., Chen S., Vecchio A., Del Pozzo W., Rosado P. A., 2021, MNRAS, 502, L99
Miranda R., Muñoz D. J., Lai D., 2017, MNRAS, 466, 1170
Moody M. S. L., Shi J.-M., Stone J. M., 2019, ApJ, 875, 66
Muñoz D. J., Miranda R., Lai D., 2019, ApJ, 871, 84
Nelson D. et al., 2015, Astron. Comput., 13, 12
Nelson D. et al., 2019, Comput. Astrophys. Cosmol., 6, 2
Nenkova M., Sirocky M. M., Nikutta R., Ivezić Ž., Elitzur M., 2008, ApJ, 685, 160
Netzer H., 2015, ARA&A, 53, 365
Netzer H., Laor A., 1993, ApJ, 404, L51
Nixon C., King A., Price D., 2013, MNRAS, 434, 1946
Nixon C., King A., Price D., Frank J., 2012, ApJ, 757, L24
Noble S. C., Krolik J. H., Campanelli M., Zlochower Y., Mundim B. C., Nakano H., Zilhão M., 2021, preprint (arXiv:2103.12100)
Paczynski B., 1977, ApJ, 216, 822
Pérez F., Granger B., 2007, Comput. Sci. Eng., 9, 21
Peters P. C., 1964, Phys. Rev., 136, 1224
Pol N. S. et al., 2021, ApJ, 911, L34
Rahvar S., Mehrabi A., Dominik M., 2011, MNRAS, 410, 912
Rajagopal M., Romani R. W., 1995, ApJ, 446, 543
Ramos Almeida C., Ricci C., 2017, Nat. Astron., 1, 679
Ricci C. et al., 2017, MNRAS, 468, 1273
Rodriguez-Gomez V. et al., 2015, MNRAS, 449, 49
Roedig C., Dotti M., Sesana A., Cuadra J., Colpi M., 2011, MNRAS, 415, 3033
Runnoe J. C. et al., 2017, MNRAS, 468, 1683
Runnoe J. C., Brotherton M. S., Shang Z., 2012, MNRAS, 422, 478
Sarajedini V. L., Gilliland R. L., Kasm C., 2003, ApJ, 599, 173
Sesana A., Haardt F., Madau P., Volonteri M., 2004, ApJ, 611, 623
Sesana A., Haiman Z., Kocsis B., Kelley L. Z., 2018, ApJ, 856, 42
Seyfert C. K., 1943, ApJ, 97, 28
Shakura N. I., Sunyaev R. A., 1973, A&A, 500, 33
Shi J.-M., Krolik J. H., 2015, ApJ, 807, 131

Sijacki D., Vogelsberger M., Genel S., Springel V., Torrey P., Snyder G. F., Nelson D., Hernquist L., 2015, MNRAS, 452, 575

Smith K. L., Mushotzky R. F., Boyd P. T., Malkan M., Howell S. B., Gelino D. M., 2018, ApJ, 857, 141

Suganuma M. et al., 2006, ApJ, 639, 46

Suh H. et al., 2019, ApJ, 872, 168

Torrey P., Vogelsberger M., Genel S., Sijacki D., Springel V., Hernquist L., 2014, MNRAS, 438, 1985

Tremmel M., Governato F., Volonteri M., Pontzen A., Quinn T. R., 2018, ApJ, 857, L22

Ueda Y., Akiyama M., Hasinger G., Miyaji T., Watson M. G., 2014, ApJ, 786, 104

Ulrich M.-H., Maraschi L., Urry C. M., 1997, ARA&A, 35, 445

Urry C. M., Padovani P., 1995, PASP, 107, 803

van der Walt S., Colbert S. C., Varoquaux G., 2011, Comput. Sci. Eng., 13, 22

Vasiliev E., Antonini F., Merritt D., 2015, ApJ, 810, 49

Vaughan S., Uttley P., Markowitz A. G., Huppenkothen D., Middleton M. J., Alston W. N., Scargle J. D., Farr W. M., 2016, MNRAS, 461, 3145

Virtanen P. et al., 2020, Nature Methods, 17, 261

Vogelsberger M. et al., 2014a, MNRAS, 444, 1518

Vogelsberger M. et al., 2014b, Nature, 509, 177

Wiktorowicz G., Middleton M., Khan N., Ingram A., Gandhi P., Dickinson H., 2021, MNRAS, 507, 374

Wyithe J. S. B., Loeb A., 2003, ApJ, 590, 691

Zrake J., Tiede C., MacFadyen A., Haiman Z., 2021, ApJ, 909, L13
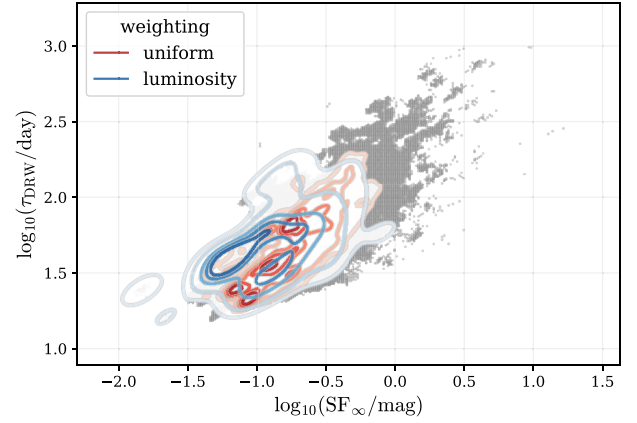
APPENDIX A: SUPPLEMENTARY MATERIAL

Figure A1. DRW parameters for the secondary MBH: contours are shown for both uniform weightings (red) and systems weighted by their luminosity (blue). The contours correspond to the quantiles: {0.10, 0.25, 0.50, 0.75, 0.90}.
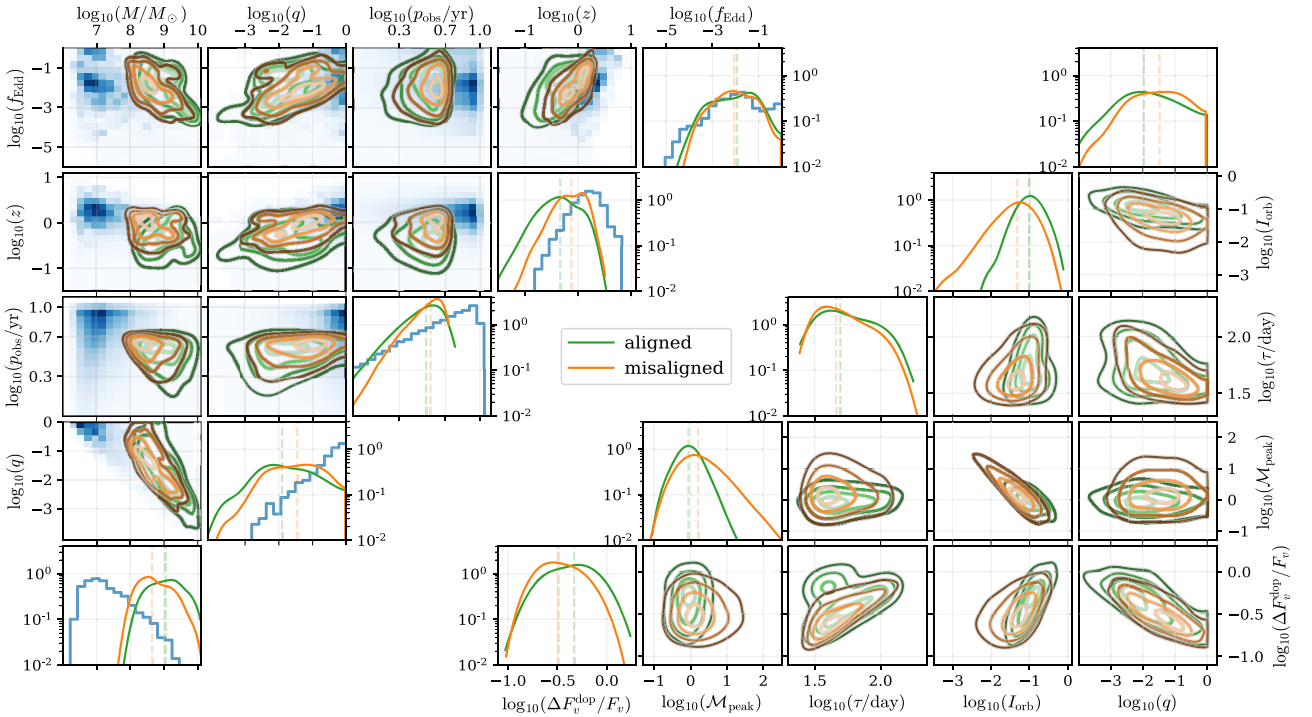

Figure A2. Binary population parameters: all simulated binaries (blue; $\approx 1.5 \times 10^6$) compared to those that are lensing-detectable aligned systems (orange) and lensing-detectable misaligned systems (green). 'Aligned' systems are those having circum-single discs coaligned with the binary orbital plane. All distributions are probability densities. The detection criteria are: a flux above 5×10^{-30} erg s^{-1} cm^{-2} Hz^{-1} in the R band, a lensing duration longer than 30 d, an observed orbital period shorter than 5 yr, and a peak lensing magnification larger than S/N^{-1} + 0.05. Lensing systems have large total masses, but relatively extreme mass ratios peaking near $q \sim 10^{-2}$. The accretion partition function, which gives the majority of mass-accretion to the secondary, allows for small overall Eddington ratios, while the Eddington ratio of the secondaries (and thus their luminosities) remain high.

Table A1. All-sky detection rates for different signals and survey parameter combinations.

Sensitivity (erg s^{-1} cm^{-2} Hz^{-1})	Period (yr)	Lensing		Doppler		Both	
		White	DRW	White	DRW	White	DRW
3×10^{-30}	3.0	$25^{+8}_{-11}\ (130^{+22}_{-20})$	$22^{+10}_{-9.0}\ (120^{+22}_{-21})$	$110^{+20}_{-20}\ (320^{+30}_{-30})$	$87^{+17}_{-17}\ (210^{+30}_{-21})$	$17^{+8.0}_{-8.0}\ (80^{+18}_{-20})$	$13^{+10}_{-6.0}\ (59^{+17}_{-13})$
	5.0	$73^{+16}_{-13}\ (510^{+31}_{-44})$	$60^{+15}_{-13}\ (450^{+32}_{-38})$	$220^{+31}_{-18}\ (670^{+51}_{-38})$	$160^{+23}_{-20}\ (370^{+36}_{-32})$	$44^{+15}_{-10}\ (250^{+32}_{-26})$	$26^{+12}_{-9.0}\ (130^{+23}_{-28})$
3×10^{-29}	3.0	$1.0^{+2.0}_{-1.0}\ (13^{+8}_{-6})$	$1.0^{+2.0}_{-1.0}\ (12^{+7}_{-6})$	$5.0^{+6.0}_{-4.0}\ (20^{+11}_{-7})$	$4.0^{+5.0}_{-3.0}\ (14^{+9}_{-6})$	$0.0^{+2.0}_{-0.0}\ (5.0^{+5.7}_{-3.0})$	$0.0^{+1.0}_{-0.0}\ (4.0^{+4.0}_{-3.0})$
	5.0	$3.0^{+3.0}_{-2.7}\ (50^{+11}_{-12})$	$2.0^{+4.0}_{-2.0}\ (47^{+10}_{-12})$	$10^{+7.0}_{-6.0}\ (44^{+13}_{-12})$	$6.0^{+6.0}_{-4.0}\ (24^{+12}_{-9.0})$	$1.0^{+3.0}_{-1.0}\ (16^{+10}_{-6.0})$	$1.0^{+1.0}_{-1.0}\ (9.0^{+6.0}_{-5.7})$

Notes. The signatures are lensing peaks, Doppler modulations, and the combination of the two (both). For each signal, we compare between a white-noise only model, and also including DRW variations that depend on the duration of a prospective signal. The first number shown in each cell assumes the secondary AGN disc is aligned with the orbital plane, while the number in parenthesis assumes a random orientation. These values do not take into account obscuration (see Section 4). Uncertainties are 2σ reflecting Poisson-like variations across 100 realizations of our binary populations with fixed parameters.

Table A2. Adopted survey parameters and number of expected detections.

Survey	$F_{\nu,\,\mathrm{sens}}$(erg s^{-1} cm^{-2} Hz^{-1})	Coverage (str./(4π))	Duration (yr)	Cadence (d)	Detections (median$^{+2\sigma}_{-2\sigma}$)
LSST	3×10^{-30}	0.8	10	3	60^{75}_{47}
CRTS	4×10^{-28}	0.8	10	7	$0^{0.8}_{0}$
PTF	2×10^{-28}	0.066	3.75	5	0^{0}_{0}
ZTF	2×10^{-28}	0.8	5	3	$0^{0.75}_{0}$
Pan-STARRS	4×10^{-29}	2×10^{-4}	5	3	0^{0}_{0}
Kepler	10^{-27}	3×10^{-3}	3.5	0.25	0^{0}_{0}
Gaia	2×10^{-28}	1.0	10	30	0^{0}_{0}

Note. The detection rates are calculate over 100 realizations of our binary populations.

This paper has been typeset from a TeX/LaTeX file prepared by the author.